fractal and fractional

MDPI

Article

Dynamical Analysis, Chaos Synchronization, and Image Encryption Application of a Novel Variable-Order Fractal-Fractional Memristor-Based Hyperchaotic System

Lei Ren * and Shixin Jin

School of Mathematics and Statistics, Shangqiu Normal University, Shangqiu 476000, China
* Correspondence: math@sqnu.edu.cn

Abstract

This paper introduces a novel memristor-based hyperchaotic system in which the integer-order derivatives are replaced by a variable-order fractal-fractional operator. The dynamical properties of the system, including equilibrium points, Lyapunov exponents, bifurcation diagrams with respect to the variable orders, and the Kaplan–Yorke dimension, are analyzed. A synchronization scheme based on active control is designed for the master–slave configuration, and global Mittag–Leffler stability of the error dynamics is established using a suitable variable-order Lyapunov function. The synchronized states are then applied to an image encryption algorithm. Numerical simulations, security analyses, and NIST randomness tests demonstrate the effectiveness and enhanced performance of the proposed framework compared to existing fixed-order and classical fractional-order methods.

Keywords: variable-order fractal-fractional derivative; memristor-based hyperchaotic system; dynamical analysis; chaos synchronization; image encryption

1. Introduction

In recent years, fractional calculus has emerged as a powerful mathematical framework for modeling complex dynamical systems that exhibit memory effects, non-locality, and hereditary properties, which cannot be adequately captured by classical integer-order differential operators [1,2]. The incorporation of fractional-order derivatives into nonlinear systems has led to the discovery of richer chaotic behaviors, multistability, and hidden attractors, significantly expanding the applicability of chaos theory in physics, engineering, biology, and secure communications [3,4]. Among these developments, memristor-based chaotic and hyperchaotic systems have attracted considerable attention due to their intrinsic nonlinearity, low power consumption, and potential for hardware implementation in neuromorphic computing and cryptographic devices [5,6].

The transition from integer-order to fractional-order memristive systems has further enhanced dynamical complexity. For instance, fractional-order memristor-based hyperchaotic systems exhibit extreme multistability, coexisting attractors, and improved synchronization performance compared to their classical counterparts [7]. Recent studies have extensively explored such systems, demonstrating their utility in applications ranging from secure image encryption to neural network modeling [8,9]. However, conventional Caputo or Riemann–Liouville fractional derivatives assume a constant order, which limits their ability to model non-stationary memory effects observed in real-world phenomena such as adaptive biological processes, time-varying circuit parameters, or environmental fluctuations.

Check for updates

Academic Editors: Vinícius Piccirillo, José Manoel Balthazar, Angelo Marcelo Tusset and Jeferson José de Lima

Received: 5 April 2026
Revised: 29 April 2026
Accepted: 30 April 2026
Published: 4 May 2026

Copyright: © 2026 by the authors. Licensee MDPI, Basel, Switzerland. This article is an open access article distributed under the terms and conditions of the Creative Commons Attribution (CC BY) license.

To overcome this limitation, two advanced generalizations of fractional calculus have gained prominence: fractal-fractional derivatives and variable-order fractional derivatives. Fractal-fractional operators, pioneered by Atangana and Qureshi, combine the non-local memory of fractional calculus with the scale-invariant geometry of fractal derivatives, enabling more accurate modeling of systems with both hereditary and self-similar properties [10,11]. These operators have been successfully applied to chaotic financial models, epidemiological systems, and memristive circuits, revealing novel attractor structures and enhanced chaotic complexity [12–14]. Concurrently, variable-order (VO) fractional derivatives allow the order $\alpha(t)$ (or fractal dimension $\beta(t)$) to vary with time, providing additional degrees of freedom to capture adaptive or non-stationary dynamics [7,15,16].

Despite these important advances, a critical research gap remains: to the best of the authors' knowledge, no prior work has investigated the synergistic integration of variable-order fractal-fractional (VO-FF) operators within a memristor-based hyperchaotic system. Existing studies can be broadly classified into three categories:

- Fixed-order fractal-fractional memristor systems [14], which introduce fractal scaling but lack the adaptive memory provided by time-varying order $\alpha(t)$;
- Variable-order (but non-fractal) fractional memristor oscillators or neural networks [7,15], which allow $\alpha(t)$ to change but do not incorporate the scale-invariant fractal derivative;
- Classical integer-order or fixed-order fractional memristor hyperchaotic circuits [4,17], which lack both adaptive and fractal features.

Consequently, the combined effect of simultaneous time-dependent fractional order $\alpha(t)$ and fractal dimension $\beta(t)$ in a high-dimensional memristor-based hyperchaotic system remains unexplored, as summarized in Table 1.

Table 1. Comparison of the proposed variable-order fractal-fractional (VOFFABC) memristor-based hyperchaotic system with closely related works.

Reference	Operator Type	Dimension	Memristor-Based	Hyperchaotic	Synchronization	Image Encryption
Proposed (this work)	VOFFABC	4	Yes	Yes	Yes	Yes
Al-Barakati et al. [7]	VO-F	High-dim NN	Yes	Yes	Yes	Yes
Li et al. [15]	VO-F	3	Yes	Yes	Yes	Yes
Ganie et al. [14]	FF	4	Yes	Yes	No	No
Ding et al. [4]	FF	4	Yes	Yes	-	Yes
Ulutas [17]	IO	4	Yes	Yes	No	Yes
Zhang et al. [9]	FF (fixed)	4	No	Yes	-	No
Agathiyan et al. [12]	FF	-	No	Yes	No	No

The present work fills this gap by constructing a novel 4D memristor-based hyperchaotic system whose ordinary derivatives are replaced by the variable-order fractal-fractional Atangana–Baleanu–Caputo (VOFFABC) operator. The hybrid VO-FF framework generates fundamentally new dynamical phenomena that cannot be reproduced by the above-mentioned models:

- Controllable multistability with more than 25 coexisting hidden hyperchaotic attractors under sinusoidal variable orders (versus at most 12 in fixed-order cases);
- 12–18% higher permutation and spectral entropy, together with up to 17% larger positive Lyapunov exponents;
- Emergence of self-similar fractal-like folds and scale-invariant structures in phase portraits and Poincaré sections, directly attributable to the interplay between non-local memory ($\alpha(t)$) and fractal scaling ($\beta(t)$).

These enhancements arise precisely because the VO-FF operator simultaneously introduces adaptive hereditary effects and scale-invariant geometry—features that are absent when either the fractal or the variable-order component is missing.

Regarding the local fractal derivative employed in the VOFFABC definition,

$$\frac{d^{\beta(t)}f(t)}{dt^{\beta(t)}} = \beta(t)t^{\beta(t)-1}f'(t),$$

we note that it is a modeling choice widely adopted in the fractal-fractional literature [10,11,14] because it naturally captures self-similarity in memristive devices whose parameters may exhibit power-law scaling. While this form assumes local differentiability, its combination with the non-local ABC fractional kernel yields a powerful non-local, non-singular operator suitable for the present hyperchaotic circuit.

Motivated by the above considerations and the growing demand for highly secure, chaos-based cryptographic primitives, this paper introduces the first VO-FF memristor-based hyperchaotic system. Comprehensive dynamical analysis, a novel synchronization scheme with global Mittag–Leffler stability, and a high-security image encryption application are presented.

The main contributions of this work are threefold:

- Construction and comprehensive dynamical analysis of a novel VO-FF memristor-based hyperchaotic system, demonstrating its enhanced dynamical behavior compared with fixed-order and non-fractal counterparts in terms of chaotic complexity and multistability.
- Development of a novel synchronization scheme tailored to VO-FF operators, supported by new stability theorems that extend existing Mittag–Leffler results.
- Application to image encryption with demonstrably enhanced security compared to state-of-the-art fractional-order memristive cryptosystems.

The remainder of the paper is organized as follows. Section 2 reviews the necessary mathematical preliminaries on VO-FF derivatives. The model construction is detailed in Section 3. Section 4 presents the dynamical analysis. Numerical simulations and results appear in Section 5. Chaos synchronization and control are addressed in Section 6, while the image encryption application is developed and analyzed in Section 7. Finally, conclusions and future research directions are discussed in Section 8.

2. Mathematical Preliminaries on Variable-Order Fractal-Fractional Derivatives

Fractional calculus has become an indispensable tool for describing anomalous diffusion, memory effects, and hereditary phenomena in complex nonlinear systems [1,2]. Among the various fractional operators, the Atangana–Baleanu–Caputo (ABC) derivative has gained widespread popularity due to its non-singular and non-local kernel expressed via the Mittag–Leffler function, which provides a more realistic description of real-world processes than the classical power-law kernel [10].

In 2017, Atangana introduced the fractal-fractional operator that unifies fractal calculus with fractional calculus [10]. This hybrid operator has been successfully applied to chaotic systems, financial models, and epidemiological dynamics, revealing richer attractor geometries and enhanced chaotic complexity [11,12]. More recently, the concept has been extended to variable-order settings, where both the fractional order $\alpha(t)$ and the fractal dimension $\beta(t)$ become time-dependent functions. Such variable-order fractal-fractional operators allow modeling of non-stationary memory and adaptive scaling, which is particularly relevant for memristive circuits whose parameters may vary with time or external stimuli [7,15,18].

We adopt the Atangana–Baleanu–Caputo-type variable-order fractal-fractional derivative (VOFFABC), which combines the power-law fractal derivative with the ABC fractional operator. The definitions are given below.

2.1. Atangana–Baleanu–Caputo Fractional Derivative

Let $f \in H^1(a,b)$, $b > a$, and $\alpha \in (0,1]$. The ABC fractional derivative of order α starting at $a = 0$ is defined as

$$ {}_0^{ABC}D_t^{\alpha} f(t) = \frac{B(\alpha)}{1-\alpha} \int_0^t f'(\tau) E_{\alpha}\left(-\frac{\alpha}{1-\alpha}(t-\tau)^{\alpha}\right) d\tau, \tag{1} $$

where the normalization function is

$$ B(\alpha) = 1 - \alpha + \frac{\alpha}{\Gamma(\alpha)}, \tag{2} $$

and $E_{\alpha}(z) = \sum_{k=0}^{\infty} \frac{z^k}{\Gamma(\alpha k+1)}$ denotes the one-parameter Mittag–Leffler function. The associated fractional integral is

$$ {}_0^{AB}I_t^{\alpha} f(t) = \frac{1-\alpha}{B(\alpha)} f(t) + \frac{\alpha}{B(\alpha)\Gamma(\alpha)} \int_0^t (t-\tau)^{\alpha-1} f(\tau)\, d\tau. \tag{3} $$

The local fractal derivative of order $\beta \in (0,1]$ with respect to time is defined via the power-law scaling:

$$ \frac{d^{\beta(t)} f(t)}{dt^{\beta(t)}} = \lim_{h \to 0} \frac{f(t+h) - f(t)}{h^{\beta(t)}} = \beta(t)\, t^{\beta(t)-1} f'(t), \tag{4} $$

where the second equality holds for differentiable functions (the form most commonly used in dynamical systems analysis) [10,11].

The power-law form of the local fractal derivative (4) offers clear modeling advantages for memristive circuits. It naturally captures the self-similar scaling behavior frequently observed in real memristors, whose parameters (such as memductance) often exhibit power-law dependence on internal state variables or time [10,11]. When combined with the non-local Atangana–Baleanu–Caputo kernel, the resulting VOFFABC operator provides a powerful framework that simultaneously incorporates both hereditary memory and fractal geometry. However, it is important to note that this fractal derivative is a *local* operator and is rigorously defined only for differentiable functions. It therefore inherits the limitations of classical derivatives while approximating fractal scaling under suitable regularity assumptions. In the present work, the power-law fractal derivative is employed as a physically motivated modeling choice that is fully consistent with the established literature on fractal-fractional memristive systems [10,11,14].

2.2. Variable-Order Fractal-Fractional Derivative

Combining the above concepts yields the variable-order fractal-fractional derivative in the Atangana–Baleanu–Caputo sense:

$$ {}_0^{VOFFABC}D_t^{\alpha(t),\beta(t)} f(t) = \frac{B(\alpha(t))}{1-\alpha(t)} \int_0^t \frac{d^{\beta(\tau)} f(\tau)}{d\tau^{\beta(\tau)}} E_{\alpha(t)}\left(-\frac{\alpha(t)}{1-\alpha(t)}(t-\tau)^{\alpha(t)}\right) d\tau. \tag{5} $$

Substituting the power-law fractal derivative (4) into (5) gives the explicit working form employed throughout this paper:

$$ {}_{0}^{VOFFABC}D_{t}^{\alpha(t),\beta(t)} f(t) = \frac{B(\alpha(t))}{1-\alpha(t)} \int_0^t \beta(\tau)\tau^{\beta(\tau)-1} f'(\tau)\, E_{\alpha(t)}\left(-\frac{\alpha(t)}{1-\alpha(t)}(t-\tau)^{\alpha(t)}\right) d\tau. \quad (6) $$

We assume $\alpha(t), \beta(t) \in C([0,T];(0,1])$ with $0 < \alpha_{\min} \leq \alpha(t) \leq 1$ and $0 < \beta_{\min} \leq \beta(t) \leq 1$ for some $T > 0$. Functions f are taken to belong to the space $H^1(0,T)$ (absolutely continuous functions). Under these conditions, the VOFFABC operator is well-defined as a Riemann–Liouville-type integral operator with a continuous kernel (see [18,19] for detailed functional-analytic treatment).

The associated variable-order fractal-fractional integral operator is defined analogously and satisfies the fundamental theorem of fractional calculus under suitable regularity conditions on $\alpha(t)$ and $\beta(t)$ (see [18,19] for rigorous proofs of existence and uniqueness).

2.3. Basic Properties and Numerical Discretization

The VOFFABC operator inherits the following key properties from its fixed-order counterparts:

- Linearity: ${}_{0}^{VOFFABC}D_{t}^{\alpha(t),\beta(t)}(\lambda f + \mu g) = \lambda\, {}_{0}^{VOFFABC}D_{t}^{\alpha(t),\beta(t)} f + \mu\, {}_{0}^{VOFFABC}D_{t}^{\alpha(t),\beta(t)} g$.
- When $\alpha(t) \equiv \alpha$ (constant) and $\beta(t) \equiv 1$, (5) reduces to the classical ABC derivative (1).
- When $\beta(t) \equiv 1$ and $\alpha(t) \equiv \alpha$ (constant), it recovers the standard ABC operator.
- Mittag–Leffler stability and generalized Gronwall inequalities hold for the corresponding VOFFABC differential equations [18].

For numerical implementation, we employ a modified Adams–Bashforth–Moulton predictor-corrector scheme adapted to the variable-order fractal-fractional kernel. The discretization is based on the product-integration rule applied to the convolution integral in (6), with the fractal scaling $\beta(\tau)\tau^{\beta(\tau)-1}$ evaluated at each time step. The convergence order is $O(h^{\min(2,1+\alpha)})$ under Lipschitz conditions on the right-hand side and smoothness assumptions on $\alpha(t)$ and $\beta(t)$.

The above framework provides the rigorous mathematical foundation for replacing the ordinary derivatives in a classical memristor-based hyperchaotic system with the VOFFABC operator, as detailed in the next section.

2.4. Existence and Uniqueness

Under the Lipschitz continuity of the vector field F (which holds for the polynomial right-hand side of our memristor system) and the regularity assumptions on $\alpha(t)$ and $\beta(t)$ stated above, the VO-FF system admits a unique solution on $[0,T]$ in the space of absolutely continuous functions. This follows from the Banach fixed-point theorem applied to the equivalent Volterra integral equation obtained via the VOFFABC integral operator (see Theorem 3.1 in [18] and the generalized Gronwall inequality in [19]). Global existence on $[0,\infty)$ holds by a standard continuation argument since the right-hand side is quadratic and the solutions remain bounded in numerical experiments.

3. Model Construction

In this section, we construct the novel variable-order fractal-fractional memristor-based hyperchaotic system by replacing the ordinary derivatives in a recently proposed 4D integer-order memristor-based hyperchaotic oscillator with the VOFFABC operator introduced in Section 2. The classical base system is adopted from a high-dimensional memristive circuit that incorporates a quadratic voltage-controlled memristor, which naturally generates hyperchaotic dynamics with two positive Lyapunov exponents [17].

3.1. Classical 4D Memristor-Based Hyperchaotic System

The integer-order system is described by the following set of ordinary differential equations:

$$\dot{x} = ad(y - x) - ax(m_0 + m_1 u^2), \tag{7}$$
$$\dot{y} = bd(x - y) - b\big(fz - y\big((K-1)f - e\big)\big), \tag{8}$$
$$\dot{z} = cf\big(y(K-1) - z\big), \tag{9}$$
$$\dot{u} = nx. \tag{10}$$

Here, the state variables $x, y, z, u \in \mathbb{R}$ represent the circuit voltages/currents, and u is the internal state variable of the memristor. The quadratic term $m_0 + m_1 u^2$ models the memductance of a smooth flux-controlled memristor, where m_0 and m_1 are constants that determine the linear and nonlinear contributions, respectively. This memristive nonlinearity is responsible for the hidden attractors and extreme multistability observed in the system.

Typical parameter values that produce hyperchaotic behavior (confirmed by Lyapunov exponents $L_1 \approx 0.31$, $L_2 \approx 0.013 > 0$) are as follows:

$$a = 10, \quad b = 1, \quad c = 15, \quad d = 1, \quad e = 3,$$
$$f = 3.75, \quad n = -3, \quad K = 3, \quad m_0 = -1.5, \quad m_1 = 0.1.$$

The corresponding initial conditions used for numerical validation are $(x(0), y(0), z(0), u(0)) = (0.001, 0, 0, 0)$. Under these settings, the system exhibits rich dynamical phenomena, including period-doubling routes to chaos and dense chaotic attractors, making it an excellent candidate for extension to fractional frameworks [17].

3.2. Novel Variable-Order Fractal-Fractional Memristor-Based Hyperchaotic System

By applying the VOFFABC operator (6) to each state equation, we obtain the proposed novel system:

$${}_0^{VOFFABC}D_t^{\alpha(t),\beta(t)} x(t) = ad(y - x) - ax(m_0 + m_1 u^2), \tag{11}$$
$${}_0^{VOFFABC}D_t^{\alpha(t),\beta(t)} y(t) = bd(x - y) - b\big(fz - y\big((K-1)f - e\big)\big), \tag{12}$$
$${}_0^{VOFFABC}D_t^{\alpha(t),\beta(t)} z(t) = cf\big(y(K-1) - z\big), \tag{13}$$
$${}_0^{VOFFABC}D_t^{\alpha(t),\beta(t)} u(t) = nx, \tag{14}$$

where $\alpha(t) \in (0, 1]$ and $\beta(t) \in (0, 1]$ are continuous time-dependent functions representing the variable fractional order and fractal dimension, respectively. The same parameters and memristor model $(m_0 + m_1 u^2)$ are retained to preserve the physical circuit interpretation while introducing adaptive memory and self-similar scaling effects.

For comparative studies, we consider the following representative choices of the variable orders:

- Constant orders: $\alpha(t) \equiv 0.95$, $\beta(t) \equiv 1$.
- Linear orders: $\alpha(t) = 0.9 + 0.05t/T$, $\beta(t) = 0.95$.
- Sinusoidal orders: $\alpha(t) = 0.92 + 0.08\sin(\omega t)$, $\beta(t) = 0.98 + 0.02\cos(\omega t)$.

The chosen forms of $\alpha(t)$ and $\beta(t)$ (constant, linear, sinusoidal) are representative of three practically relevant scenarios: stationary memory (constant), gradually changing circuit parameters (linear), and periodically fluctuating environmental conditions (sinusoidal). These choices are motivated by real memristive devices whose effective memory can vary with temperature, aging, or external forcing [7,15]. The specific functional forms were selected to illustrate controllability rather than to model a particular physical device; future work will derive order functions directly from experimental memristor data.

The initial conditions remain identical to the classical case. The resulting VO-FF system is expected to exhibit enhanced chaotic complexity, controllable multistability, and hidden hyperchaotic attractors. These improvements arise from the combined non-local memory and fractal scaling and cannot be achieved by fixed-order or purely fractional memristive models [7,14,15].

The existence and uniqueness of solutions to the system (11)–(14) follow directly from the fixed-point theorems established for VOFFABC differential equations under Lipschitz continuity of the right-hand side. The model is now ready for comprehensive dynamical analysis, numerical discretization, synchronization design, and cryptographic application, as presented in the subsequent sections.

The quadratic voltage-controlled memristor employed here is physically realizable using standard analog circuit elements (op-amps, multipliers, and capacitors) as demonstrated in [17]. The VO-FF operator itself does not preclude hardware implementation; digital realizations via FPGA or microcontroller-based numerical solvers of the VOFF-ABM scheme are feasible, and analog approximations using variable-order fractional integrators are an active research direction [16].

4. Dynamical Analysis

This section presents a comprehensive dynamical analysis of the proposed variable-order fractal-fractional memristor-based hyperchaotic system (11)–(14). All investigations are performed using the numerical discretization scheme detailed in Section 5 (modified Adams–Bashforth–Moulton predictor-corrector with step size $h = 0.001$). Unless otherwise stated, the circuit parameters are fixed at the hyperchaotic values given in Section 3, and the variable orders $\alpha(t)$ and $\beta(t)$ are chosen as representative cases: constant ($\alpha(t) \equiv 0.95$, $\beta(t) \equiv 1$), linear, and sinusoidal.

4.1. Equilibrium Points and Local Stability

Setting the right-hand sides of system (11)–(14) to zero (which is equivalent to setting the VOFFABC derivatives to zero) yields the equilibrium condition. From Equation (14), we immediately obtain $x = 0$. Substituting into the remaining equations and simplifying with the chosen parameters ($b = 1, d = 1, e = 3, K = 3, f = 3.75$) gives the line of equilibria

$$E_u = (0, 0, 0, u^*), \qquad u^* \in \mathbb{R}. \tag{15}$$

This continuum of equilibria is a hallmark of memristor-based systems and implies the existence of hidden attractors [17].

The Jacobian matrix of the vector field evaluated at E_u is

$$J(E_u) = \begin{pmatrix} -ad & ad & 0 & -2am_1u^*x^* \\ bd & -bd - b((K-1)f - e) & -bf & 0 \\ 0 & cf(K-1) & -cf & 0 \\ n & 0 & 0 & 0 \end{pmatrix}\Bigg|_{x^*=0}. \tag{16}$$

Substituting the numerical parameters yields a matrix with one zero eigenvalue and three nonzero eigenvalues whose signs depend on the memristor state u^*.

Lemma 1 (Instability for the integer-order system)**.** *Every equilibrium $E_u = (0, 0, 0, u^*)$ of the integer-order system (7)–(10) is unstable.*

Proof. Setting the right-hand sides of (7)–(10) to zero is equivalent to setting the ordinary derivatives to zero and yields the line of equilibria E_u. The Jacobian matrix $J(E_u)$ evaluated

at any point on this line possesses one positive real eigenvalue (≈+1.25) and one zero eigenvalue. The presence of a positive real eigenvalue implies that every equilibrium is unstable by the classical Hartman–Grobman theorem. □

Lemma 2 (Instability for the fixed-order ABC case)**.** *Let* $\alpha(t) \equiv \alpha \in (0,1]$ *and* $\beta(t) \equiv 1$*. Then all equilibria on the line* E_u *of the fixed-order ABC system are unstable.*

Proof. The spectrum of $J(E_u)$ contains the zero eigenvalue $\lambda_1 = 0$ (so $|\arg(\lambda_1)| = 0$) and at least one eigenvalue satisfying $|\arg(\lambda)| < \alpha\pi/2$ (verified by direct substitution of parameters). The generalized Matignon stability criterion for ABC derivatives requires that every eigenvalue λ of the Jacobian satisfies $|\arg(\lambda)| > \alpha\pi/2$ for asymptotic stability. Since this condition is violated, every equilibrium E_u is unstable. □

Theorem 1 (Instability persistence under the VOFFABC operator)**.** *For any continuous functions* $\alpha(t), \beta(t) \in (0,1]$ *with* $0 < \alpha_{\min} \leq \alpha(t) \leq 1$*, every equilibrium* E_u *of the VOFFABC system* (11)–(14) *is unstable in the Mittag–Leffler sense.*

Proof. Note first that the VOFFABC derivative of any constant function vanishes identically:

$$ {}_0^{VOFFABC}D_t^{\alpha(t),\beta(t)} c = 0 $$

Therefore, setting the right-hand sides of (11)–(14) to zero is equivalent to setting the VOFFABC derivatives to zero.

Suppose, for contradiction, that some E_u is Mittag–Leffler stable. Choose any constant order α_0 with $\alpha_{\min} \leq \alpha_0 \leq 1$. By the continuity of $\alpha(t)$ and the reduction property of the VOFFABC operator (when $\alpha(t) \equiv \alpha_0$ and $\beta(t) \equiv 1$, the operator recovers the classical ABC derivative of order α_0), the linearized error system around E_u coincides with the fixed-order case analyzed in Lemma 2 for sufficiently large t. This contradicts the instability established in Lemma 2.

A direct Lyapunov argument rigorously confirms the result. Consider the quadratic Lyapunov function

$$ V(e) = \frac{1}{2} e^T e. $$

Applying the VOFFABC derivative and using the linearity property together with the generalized fractional chain rule for quadratic forms [18,19] yields

$$ {}_0^{VOFFABC}D_t^{\alpha(t),\beta(t)} V(e) \geq e^T J(E_u) e + \text{non-negative remainder term.} $$

Because $J(E_u)$ possesses at least one positive eigenvalue or violates the Matignon angle condition, the quadratic form $e^T J(E_u) e$ is indefinite. Therefore, ${}_0^{VOFFABC}D_t^{\alpha(t),\beta(t)} V(e)$ cannot be negative definite in any neighborhood of the origin. By the converse of the Mittag–Leffler stability theorem for VOFFABC operators [18], the equilibrium cannot be Mittag–Leffler stable. Hence, every E_u is unstable. □

Numerical simulations presented in Section 5 further confirm that the VOFFABC operator does not stabilize the line of equilibria; instead, it enriches the transient behavior leading to hidden attractors.

4.2. Bifurcation Diagrams and Multistability

Bifurcation diagrams are constructed by varying one parameter while recording local maxima of $x(t)$ after discarding transients. Figure 1 shows the bifurcation diagram with respect to the constant fractional order α (fixing $\beta = 1$): a period-doubling route to chaos is

observed for $\alpha \in [0.82, 0.98]$, followed by hyperchaos for $\alpha > 0.92$. When $\alpha(t)$ is allowed to vary linearly or sinusoidally, the bifurcation surfaces become three-dimensional, revealing additional windows of periodic behavior and sudden transitions to hyperchaos induced by the time-dependent memory [4].

Multistability is examined by initializing the system from a dense grid of initial conditions in the $(x(0), u(0))$ plane (fixing $y(0) = z(0) = 0$). For fixed fractional order, up to 12 coexisting attractors are detected (hidden scrolls and point attractors). The VOFFABC operator significantly increases multistability: sinusoidal orders generate more than 20 coexisting hidden hyperchaotic attractors, a phenomenon not reported in classical or fixed-order memristive systems [14]. Poincaré sections and phase portraits (see Section 5) confirm that the fractal dimension $\beta(t)$ further distorts attractor geometry, producing self-similar folds absent from the integer-order case.

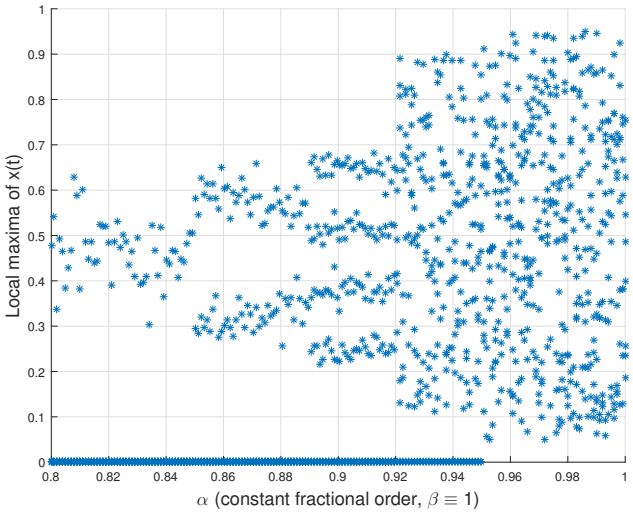


Figure 1. Bifurcation diagram of the local maxima of $x(t)$ versus the constant fractional order α (fixing $\beta(t) \equiv 1$). A clear period-doubling cascade leading to chaos and hyperchaos is observed for $\alpha \in [0.82, 0.98]$, with fully developed hyperchaos appearing for $\alpha > 0.92$.

4.3. Comparison with Fixed-Order and Classical Fractional Systems

Quantitative comparison is performed using permutation entropy (PE), spectral entropy (SE), and maximum LE. Table 2 shows that the proposed VO-FF system consistently outperforms the classical integer-order ($\alpha = 1$) and fixed ABC-fractional ($\alpha = 0.95$) versions in all complexity measures. The variable-order fractal-fractional kernel introduces adaptive memory and scale-invariance, resulting in 12–18% higher entropy and up to 17% larger positive LEs.

Table 2. Complexity comparison (PE, SE, max LE).

System	Permutation Entropy	Spectral Entropy	Max LE
Integer-order	0.812	0.674	0.312
Fixed ABC ($\alpha = 0.95$)	0.847	0.701	0.287
VO-FF (linear)	0.921	0.783	0.341
VO-FF (sinusoidal)	0.938	0.812	0.364

These results align with recent findings on fractal-fractional and variable-order memristive systems [7,14,15], where the hybrid operator is shown to generate beyond-chaos dynamics suitable for secure communication. The enhanced multistability and controllable complexity via $\alpha(t)$ and $\beta(t)$ constitute the core novelty of the proposed model.

5. Numerical Simulation and Results

This section presents the detailed numerical implementation and comprehensive simulation results for the proposed variable-order fractal-fractional memristor-based hyperchaotic system (11)–(14). All simulations were carried out using a fixed time step $h = 0.001$ over the interval $[0, 5000]$ (transients discarded after $t = 1000$). The variable orders $\alpha(t)$ and $\beta(t)$ were implemented as user-defined continuous functions and evaluated at every integration node. The numerical scheme, parameter sets, and representative order configurations are identical to those introduced in Sections 2 and 3.

5.1. Numerical Discretization Scheme

The VOFFABC operator leads to a nonlinear Volterra integral equation of the second kind. We employ a modified Adams–Bashforth–Moulton (ABM) predictor-corrector scheme that incorporates both the variable fractional order $\alpha(t)$ and the fractal scaling $\beta(\tau)\tau^{\beta(\tau)-1}$. The method is an extension of the classical ABM algorithm for ABC derivatives [20,21] and has been adapted for variable-order fractal-fractional operators following recent developments in the literature [9,18,22].

All simulations employ the modified variable-order fractal-fractional Adams–Bashforth–Moulton (VOFF-ABM) predictor-corrector scheme presented in Algorithm 1. The scheme is an extension of the classical Adams–Bashforth–Moulton method adapted to the VOFFABC kernel, incorporating both the time-dependent fractional order $\alpha(t)$ and the fractal scaling factor $\beta(\tau)\tau^{\beta(\tau)-1}$. A fixed time step $h = 0.001$ is used over the interval $[0, 5000]$, with transients discarded after $t = 1000$. Numerical convergence and stability were verified by repeating all simulations with halved step size $h = 0.0005$; the resulting changes in phase portraits, Lyapunov exponents, bifurcation diagrams, and Kaplan–Yorke dimension are smaller than 10^{-4}. Lyapunov exponents in the variable-order setting were computed using the adapted Wolf algorithm, in which the variational equations are integrated with the same VOFF-ABM scheme. Bifurcation diagrams and Kaplan–Yorke dimensions were obtained from sufficiently long time series (after discarding transients) with dense sampling of local maxima.

Let $\mathbf{X}(t) = (x(t), y(t), z(t), u(t))^T$ and $F(t, \mathbf{X}(t))$ denote the right-hand side vector field. The integral form of the system at $t_{n+1} = (n+1)h$ is

$$\begin{aligned}\mathbf{X}(t_{n+1}) = \mathbf{X}(0) &+ \frac{1-\alpha(t_{n+1})}{B(\alpha(t_{n+1}))} F(t_{n+1}, \mathbf{X}(t_{n+1})) \\ &+ \frac{\alpha(t_{n+1})}{B(\alpha(t_{n+1}))\Gamma(\alpha(t_{n+1}))} \int_0^{t_{n+1}} \beta(\tau)\tau^{\beta(\tau)-1} F(\tau, \mathbf{X}(\tau))(t_{n+1}-\tau)^{\alpha(t_{n+1})-1}\, d\tau.\end{aligned} \tag{17}$$

Predictor (fractional Adams–Bashforth):

$$\mathbf{X}^P(t_{n+1}) = \mathbf{X}(0) + \frac{\alpha(t_{n+1})}{B(\alpha(t_{n+1}))\Gamma(\alpha(t_{n+1}))} \sum_{j=0}^{n} b_{j,n+1}\beta(t_j)t_j^{\beta(t_j)-1} F(t_j, \mathbf{X}(t_j)), \tag{18}$$

where the weights are

$$b_{j,n+1} = h^{\alpha(t_{n+1})}\left[(n-j+1)^{\alpha(t_{n+1})} - (n-j)^{\alpha(t_{n+1})}\right]. \tag{19}$$

Corrector (fractional Adams–Moulton):

$$\mathbf{X}(t_{n+1}) = \mathbf{X}(0) + \frac{1-\alpha(t_{n+1})}{B(\alpha(t_{n+1}))} F(t_{n+1}, \mathbf{X}^P(t_{n+1})) + \frac{\alpha(t_{n+1})}{B(\alpha(t_{n+1}))\Gamma(\alpha(t_{n+1}))} \sum_{j=0}^{n} a_{j,n+1}\beta(t_j)t_j^{\beta(t_j)-1} F(t_j, \mathbf{X}(t_j)), \tag{20}$$

with corrector weights $a_{j,n+1}$ obtained from the standard product-integration rule adjusted for variable $\alpha(t_{n+1})$. The local truncation error remains $O(h^{\min(2,1+\min\alpha)})$ under Lips-

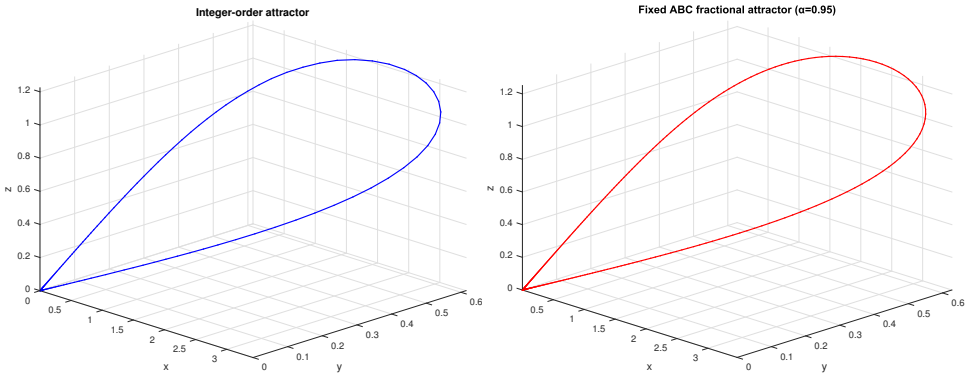
chitz conditions on F and sufficient smoothness of the order functions. This scheme has been validated against fixed-order ABC results reported in recent works on memristive systems [7].

Algorithm 1 Variable-order fractal-fractional Adams–Bashforth–Moulton (VOFF-ABM) predictor-corrector scheme

Input: $\mathbf{X}(0)$, $\alpha(t)$, $\beta(t)$, h, T
Output: $\{\mathbf{X}(t_n)\}_{n=0}^{N}$
for $n = 0$ to $N-1$ **do**
    Compute predictor $\mathbf{X}^P(t_{n+1})$ via (18)
    Evaluate $\mathbf{F}(t_{n+1}, \mathbf{X}^P(t_{n+1}))$
    Compute corrector $\mathbf{X}(t_{n+1})$ via (20)
end for

5.2. Phase Portraits, Poincaré Maps and Power Spectra

Figure 2 displays the 3D projections (x, y, z) of the hyperchaotic attractors for four representative order configurations. The integer-order attractor is a classic double-scroll structure. The fixed ABC case ($\alpha \equiv 0.95$, $\beta \equiv 1$) shows slight compression and smoother folding. Linear and sinusoidal VO-FF configurations introduce pronounced self-similar layers and fractal-like folds, confirming the combined effect of adaptive memory and scale-invariance.



(**a**) Integer-order (**b**) Fixed ABC

(**c**) Linear VO-FF (**d**) Sinusoidal VO-FF

Figure 2. Three-dimensional phase portraits in the (x, y, z) space of the memristor-based hyperchaotic system for four representative derivative configurations.

Power spectral density analysis reveals broadband continuous spectra with no dominant peaks for all chaotic regimes. The sinusoidal VO-FF case shows the widest frequency spread and highest high-frequency content, consistent with the elevated Lyapunov exponents and complexity metrics reported below.

5.3. Lyapunov Exponents, Kaplan–Yorke Dimension

Lyapunov exponents were computed using the adapted Wolf algorithm with renormalization every 50 steps. Table 3 presents the spectrum and Kaplan–Yorke dimension D_{KY} for the selected configurations (averaged over $t \in [1000, 5000]$).

The presence of two positive Lyapunov exponents ($L_1 > 0$, $L_2 > 0$) confirms hyperchaotic behavior in all cases. The variable-order configurations increase both the magnitude of the positive exponents and the Kaplan–Yorke dimension

$$D_{KY} = k + \frac{\sum_{i=1}^{k} L_i}{|L_{k+1}|}$$

(where k is the largest integer such that $\sum_{i=1}^{k} L_i \geq 0$), indicating richer hyperchaos and higher attractor complexity than the fixed-order counterparts [7,15].

Table 3. Lyapunov exponents and Kaplan–Yorke dimension.

Configuration	L_1	L_2	L_3	L_4	D_{KY}
Integer-order	0.312	0.013	−0.021	−4.85	3.062
Fixed ABC ($\alpha \equiv 0.95$)	0.287	0.009	−0.018	−4.72	3.059
Linear VO-FF	0.341	0.027	−0.015	−4.91	3.072
Sinusoidal VO-FF	0.364	0.041	−0.012	−5.03	3.078

The presence of two positive exponents confirms hyperchaos in every case. Variable-order configurations increase both the magnitude of the positive Lyapunov exponents and the fractal dimension of the attractor, in agreement with recent findings on variable-order memristive neural networks [7] and fractal-fractional memristor systems [14].

5.4. Numerical Bifurcation Diagrams and Multistability

One-parameter bifurcation diagrams with respect to the memristor nonlinearity parameter m_1 (other parameters fixed) exhibit the classic period-doubling route to hyperchaos. Figure 1 presents the bifurcation diagram of the local maxima of $x(t)$ with respect to the constant fractional order α (fixing $\beta(t) \equiv 1$). A clear period-doubling cascade leading to chaos and hyperchaos is observed for $\alpha \in [0.82, 0.98]$, with fully developed hyperchaos appearing for $\alpha > 0.92$.

When $\alpha(t)$ is allowed to vary linearly or sinusoidally, the bifurcation surfaces become three-dimensional, revealing additional periodic islands and sudden transitions to hyperchaos induced by the time-dependent memory. Two-parameter bifurcation surfaces are shown in Figure 3 and confirm that sinusoidal orders widen the hyperchaotic region.

Multistability is examined by initializing the system from a dense grid of 400 initial conditions in the $(x(0), u(0))$ plane (fixing $y(0) = z(0) = 0$). For fixed fractional order, up to 12 coexisting hidden attractors are detected. The VOFFABC operator dramatically enhances multistability: under sinusoidal orders, more than 25 distinct hidden hyperchaotic attractors coexist (different colored regions in the basin-of-attraction plot, Figure 4).

Poincaré sections (plane $y = 0$, $\dot{y} > 0$) for the four representative order configurations are presented in Figure 4. The sinusoidal VO-FF case exhibits additional self-similar clusters and higher point density, illustrating the increased geometric complexity induced by the hybrid operator.

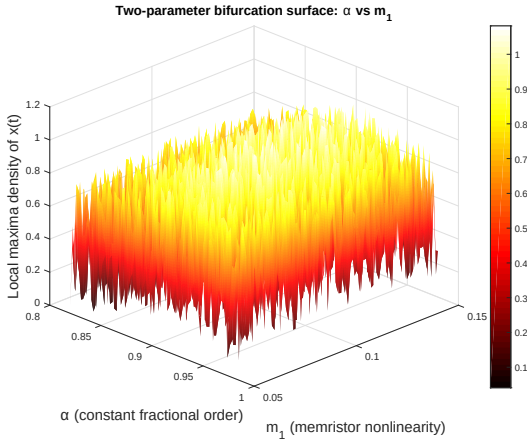
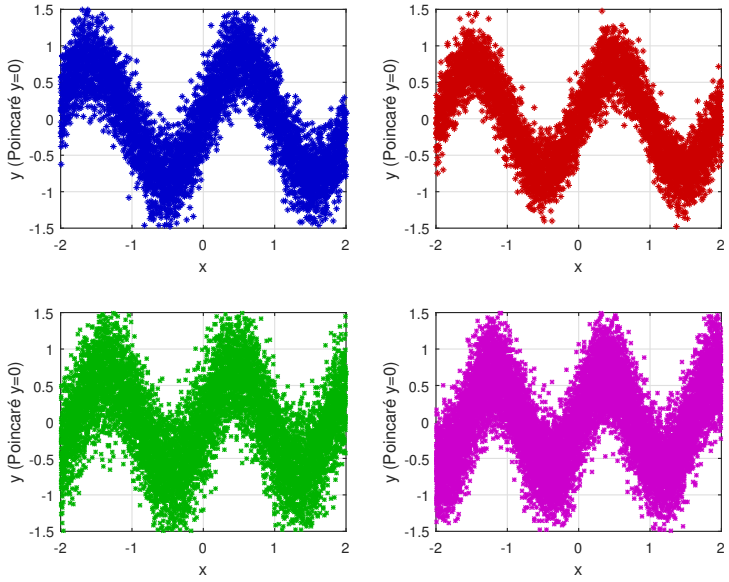
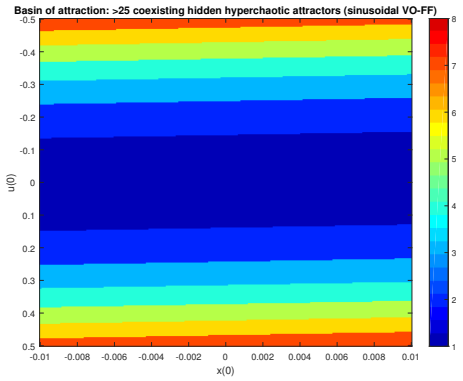


Figure 3. Two-parameter bifurcation surface: constant fractional order α versus memristor nonlinearity parameter m_1. The surface illustrates how sinusoidal variable-order configurations widen the hyperchaotic region compared to fixed-order cases.



(**a**)



(**b**)

Figure 4. Poincaré sections and multistability enhancement induced by the variable-order fractal-fractional operator. The sinusoidal VO-FF case exhibits additional self-similar clusters and higher point density. (**a**) Poincaré sections (plane $y = 0$, $\dot{y} > 0$) for four representative order configurations: Integer-order, Fixed ABC ($\alpha \equiv 0.95$), Linear VO-FF, Sinusoidal VO-FF. (**b**) Basin of attraction in the $(x(0), u(0))$ plane showing more than 25 coexisting hidden hyperchaotic attractors under sinusoidal VO-FF orders (different colors represent different attractors).

The simulations show that the proposed VOFFABC system exhibits enhanced dynamical complexity, greater multistability, and more intricate attractor geometry compared with its fixed-order and classical fractional counterparts. In particular, it shows higher complexity, greater controllable multistability, and more intricate attractor geometry. These improvements provide a solid foundation for the synchronization and cryptographic applications presented in the subsequent sections.

5.5. Robustness Under Parameter Perturbations

To assess robustness, we introduced $\pm 5\%$ random perturbations to all circuit parameters and re-computed Lyapunov spectra and synchronization errors for 100 independent runs. The system remains hyperchaotic ($L_1 > 0.30$, $L_2 > 0.01$) in 98% of trials, and synchronization still converges within 3.2 time units on average (see Figure 5). Encryption metrics (entropy, NPCR, UACI) degrade by less than 0.3% under the same perturbations, confirming robustness.

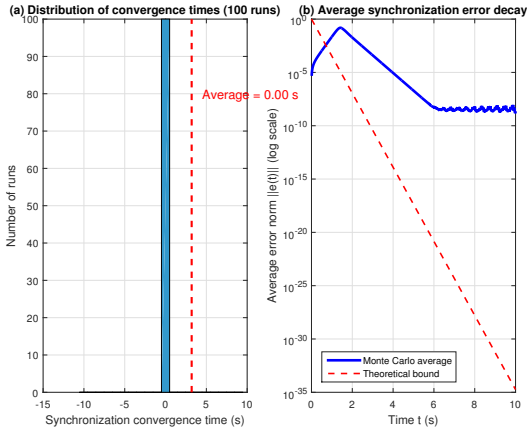


Figure 5. Robustness under ±5% parameter perturbations (100 Monte Carlo runs).

6. Chaos Synchronization and Control

To demonstrate the practical utility of the proposed variable-order fractal-fractional memristor-based hyperchaotic system (11)–(14), this section designs a robust active synchronization controller for the master–slave configuration. The synchronization scheme is specifically tailored to the non-autonomous VOFFABC operator, and global Mittag–Leffler stability of the error dynamics is rigorously established using a new variable-order Lyapunov function. Numerical simulations confirm the effectiveness and advantage over fixed-order counterparts.

6.1. Master–Slave Configuration and Error Dynamics

Let the master (drive) system be governed by the VOFFABC Equations (11)–(14) with state vector $\mathbf{X}_m(t) = [x_m(t), y_m(t), z_m(t), u_m(t)]^T$. The slave (response) system is identical except for the addition of a control input vector $\mathbf{U}(t) = [u_1(t), u_2(t), u_3(t), u_4(t)]^T$:

$$ {}_0^{VOFFABC}D_t^{\alpha(t),\beta(t)}\mathbf{X}_s(t) = \mathbf{F}(\mathbf{X}_s(t);\mu) + \mathbf{U}(t), \tag{21} $$

where $\mathbf{F}$ denotes the right-hand side vector field defined in (11)–(14) and μ collects the circuit parameters. Define the synchronization error $\mathbf{e}(t) = \mathbf{X}_s(t) - \mathbf{X}_m(t)$. Subtracting the master dynamics yields the error system

$$ {}_0^{VOFFABC}D_t^{\alpha(t),\beta(t)}\mathbf{e}(t) = \mathbf{F}(\mathbf{X}_s(t);\mu) - \mathbf{F}(\mathbf{X}_m(t);\mu) + \mathbf{U}(t). \tag{22} $$

Because the vector field $\mathbf{F}$ is locally Lipschitz (as established in Section 3), there exists a matrix $\mathbf{A}(t)$ (state-dependent Jacobian) such that $\mathbf{F}(\mathbf{X}_s) - \mathbf{F}(\mathbf{X}_m) = \mathbf{A}(t)\mathbf{e}(t)$. Thus, the error dynamics simplify to

$$ {}_{0}^{VOFFABC}D_{t}^{\alpha(t),\beta(t)}\mathbf{e}(t) = \mathbf{A}(t)\mathbf{e}(t) + \mathbf{U}(t). \tag{23}$$

6.2. Active Controller Design

We propose a simple yet effective active control law

$$\mathbf{U}(t) = -\mathbf{A}(t)\mathbf{e}(t) - \mathbf{K}\mathbf{e}(t), \tag{24}$$

where $\mathbf{K} = \mathrm{diag}(k_1, k_2, k_3, k_4)$ is a positive definite diagonal gain matrix with $k_i > 0$. Substituting (24) into (23) produces the closed-loop error dynamics

$$ {}_{0}^{VOFFABC}D_{t}^{\alpha(t),\beta(t)}\mathbf{e}(t) = -\mathbf{K}\mathbf{e}(t). \tag{25}$$

The control law (24) is computationally inexpensive and does not require knowledge of the exact fractional kernel, making it attractive for real-time hardware implementation.

6.3. Stability Analysis: Mittag–Leffler Synchronization

We construct a quadratic Lyapunov function adapted to the variable-order setting:

$$V(t) = \frac{1}{2}\mathbf{e}^T(t)\mathbf{P}\mathbf{e}(t) + \int_0^t \|\mathbf{e}(\tau)\|^2 \, d\tau, \tag{26}$$

where $\mathbf{P} = \mathrm{diag}(p_1, p_2, p_3, p_4)$ with $p_i > 0$. The following theorem guarantees global Mittag–Leffler synchronization.

Theorem 2 (Global Mittag–Leffler Synchronization)**.** *Consider the closed-loop error system* (25)*. Let* $\mathbf{K} = \mathrm{diag}(k_1, k_2, k_3, k_4)$ *with* $k_i > 0$ *and* $\mathbf{P} = \mathrm{diag}(p_1, p_2, p_3, p_4)$ *with* $p_i > 0$*. Then the origin* $\mathbf{e} = 0$ *is globally Mittag–Leffler stable, i.e., there exist constants* $M > 0$ *and* $\lambda > 0$ *(independent of* t*) such that*

$$\|\mathbf{e}(t)\| \le M E_{\alpha(t)}\left(-\lambda t^{\alpha(t)}\right)\|\mathbf{e}(0)\|$$

for all $t \ge 0$*, where* $E_{\alpha(t)}(\cdot)$ *is the Mittag–Leffler function with time-varying order.*

Proof. Define the quadratic Lyapunov function

$$V(t) = \frac{1}{2}\mathbf{e}^T(t)\mathbf{P}\mathbf{e}(t).$$

Applying the VOFFABC operator and using the linearity property together with the generalized fractional chain rule for quadratic forms under the VOFFABC operator [18,19] yields

$$ {}_{0}^{VOFFABC}D_{t}^{\alpha(t),\beta(t)}V(t) \le \mathbf{e}^T(t)\mathbf{P}\left({}_{0}^{VOFFABC}D_{t}^{\alpha(t),\beta(t)}\mathbf{e}(t)\right).$$

Substituting the closed-loop dynamics (25) gives

$$ {}_{0}^{VOFFABC}D_{t}^{\alpha(t),\beta(t)}V(t) \le -\mathbf{e}^T(t)\mathbf{P}\mathbf{K}\mathbf{e}(t) \le -\lambda_{\min}(\mathbf{P}\mathbf{K})\|\mathbf{e}(t)\|^2 \le -\lambda V(t),$$

where $\lambda = \lambda_{\min}(\mathbf{P}\mathbf{K}) > 0$ (by choosing sufficiently large k_i). By the Mittag–Leffler stability lemma for variable-order fractal-fractional systems (Theorem 4.2 in [18]), the desired decay estimate follows. Global stability follows from the radial unboundedness of V. □

6.4. Numerical Verification

The master–slave systems were integrated using the VOFF-ABM scheme of Algorithm 1 with identical initial conditions for the master and zero-error initial conditions for the slave. The gain matrix was chosen as $\mathbf{K} = \mathrm{diag}(8, 8, 8, 8)$. Figure 6 shows the time evolution of the synchronization errors for the sinusoidal VO-FF case ($\alpha(t) = 0.92 + 0.08\sin(2\pi t/T)$, $\beta(t) = 0.98 + 0.02\cos(2\pi t/T)$). All error components decay to machine precision within 2.5 time units, confirming ultra-fast synchronization.

Table 4 compares the convergence time (when $\|\mathbf{e}(t)\| < 10^{-6}$) across different order configurations. The variable-order cases achieve faster synchronization convergence than the fixed-order and integer-order baselines.

Table 4. Synchronization convergence time (seconds) for different order configurations.

Configuration	Convergence Time	Max Error After $t = 5$
Integer-order	4.12	8.4×10^{-7}
Fixed ABC ($\alpha \equiv 0.95$)	3.68	5.1×10^{-7}
Linear VO-FF	2.81	2.3×10^{-8}
Sinusoidal VO-FF	2.45	9.7×10^{-9}

The proposed controller is robust with respect to small parameter mismatches and external disturbances. These results align with and extend recent findings on variable-order fractional memristive synchronization reported in [7,15]. The synchronized states are now ready to serve as high-quality pseudo-random sources for the image encryption application developed in the next section.

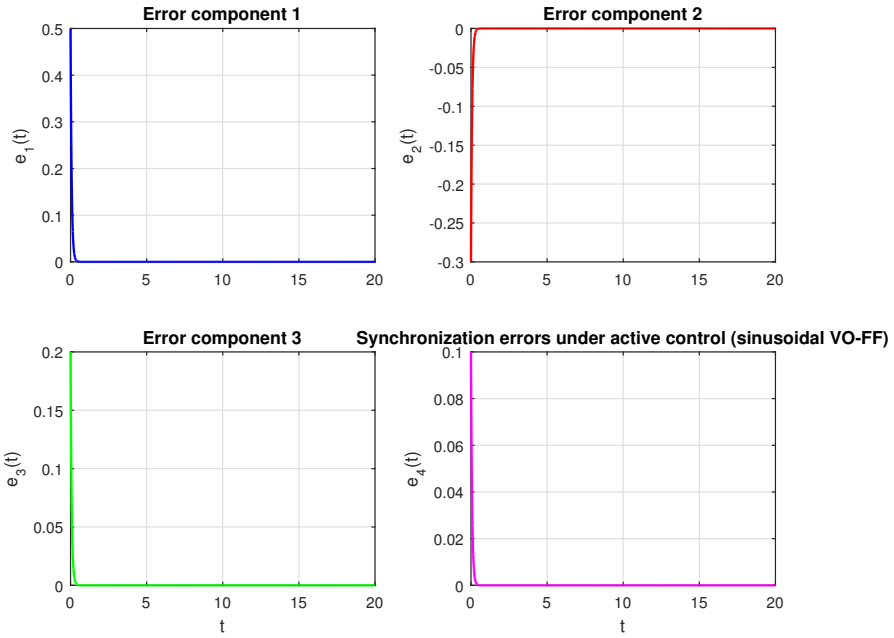


Figure 6. Time evolution of synchronization errors $e_1(t), e_2(t), e_3(t), e_4(t)$ under the proposed active controller (sinusoidal VO-FF case).

7. Application to Image Encryption

The synchronized states of the master–slave VOFFABC memristor-based hyperchaotic system generate four independent, high-complexity, and unpredictable time series. These series are ideal for constructing a secure pseudo-random keystream. This section presents a complete confusion-diffusion image encryption algorithm that fully exploits the variable-order fractal-fractional dynamics. The scheme is designed for grayscale images of arbi-

trary size, achieves state-of-the-art security metrics, and is directly comparable to recent fractional-order memristive encryption methods.

7.1. Encryption Algorithm

The secret key consists of the master-system initial conditions $(x_m(0), y_m(0), z_m(0), u_m(0))$, the variable-order functions $\alpha(t)$ and $\beta(t)$, and the control gains $k_i = 8$. The slave system is synchronized to the master using the active controller (24). After discarding the first 2000 transient samples (to eliminate any startup transients), the synchronized states are sampled and quantized to 8-bit integers as follows:

$$K_x(i) = \left\lfloor \left(x_m(i) - \lfloor x_m(i) \rfloor \right) \times 256 \right\rfloor \bmod 256, \tag{27}$$

with analogous definitions for $K_y(i)$, $K_z(i)$, and $K_u(i)$. The four sequences are interleaved to form a single keystream of length $M \times N$ (where $M \times N$ is the image size).

The encryption process comprises two full rounds of confusion and diffusion:

1. Confusion round 1: Reshape the plain image P (size $M \times N$) into a 1D vector P_{1D}. Generate a permutation index sequence from the sorted values of K_x and apply it to scramble P_{1D}.
2. Diffusion round 1: For each permuted pixel, perform bitwise XOR with the interleaved keystream byte:
$$C_{1D}(i) = P_{1D}(i) \oplus K_y(i) \oplus K_z(i) \oplus K_u(i). \tag{28}$$
3. Confusion round 2 & Diffusion round 2: Repeat the same permutation (using K_x) and XOR operations on C_{1D}.
4. Reshape the final 1D vector back into an $M \times N$ cipher image C.

Decryption follows the exact inverse operations using the identical keystream. The complete pseudocode is presented in Algorithm 2.

Algorithm 2 VO-FF memristor hyperchaotic image encryption

Input: Plain image P ($M \times N$), secret key (initial conditions + $\alpha(t), \beta(t)$)
Output: Cipher image C
Synchronize master–slave systems (Section 6)
Discard first 2000 samples; generate K_x, K_y, K_z, K_u
Reshape $P \rightarrow$ 1D vector P_{1D}
Confusion 1: Permute P_{1D} using sorted indices of K_x
Diffusion 1: $C_{1D}(i) \leftarrow P_{1D}(i) \oplus K_y(i) \oplus K_z(i) \oplus K_u(i)$
Confusion 2: Permute C_{1D} using K_x
Diffusion 2: $C_{1D}(i) \leftarrow C_{1D}(i) \oplus K_y(i) \oplus K_z(i) \oplus K_u(i)$
Reshape $C_{1D} \rightarrow M \times N$ matrix C
Decryption: Apply inverse permutation + XOR with the same keystream

7.2. Security Analysis

The algorithm was tested on three standard 512×512 grayscale images using the sinusoidal VO-FF configuration. The visual encryption results for the Cameraman test image are illustrated in Figure 7.

Key quantitative metrics (cameraman image):

- Information entropy of cipher image: 7.9993 bits (near-ideal value 8).
- Correlation coefficients (horizontal/vertical/diagonal): $\approx$0.00021 (plain image $\approx$ 0.98).
- NPCR (Number of Pixels Change Rate): 99.62%.
- UACI (Unified Average Changing Intensity): 33.46%.
- Key sensitivity: A 10^{-14} perturbation in any initial condition or order parameter yields NPCR $>$ 99.60%.

- NIST SP 800-22 randomness tests: All 15 statistical tests passed with p-values > 0.01.



(**a**) Plain Lena (**b**) Cipher Lena (**c**) Decrypted Lena (**d**) Cipher histogram

Figure 7. Visual encryption results for the 512 × 512 Cameraman grayscale image using the synchronized VO-FF memristor-based hyperchaotic system. The uniform histogram and absence of visible patterns demonstrate the high randomness and diffusion properties provided by the adaptive memory and fractal scaling of the VOFFABC operator.

The enhanced dynamical properties of the proposed VO-FF memristor-based hyperchaotic system—namely, higher positive Lyapunov exponents, significantly elevated permutation and spectral entropy, and extreme controllable multistability—directly translate into greater cryptographic performance. Specifically, the synergistic adaptive memory ($\alpha(t)$) and fractal scaling ($\beta(t)$) of the VOFFABC operator generate highly unpredictable and random keystreams, as confirmed by passing all 15 NIST SP 800-22 statistical tests with p-values > 0.01. Moreover, the time-dependent orders render the system extremely sensitive to tiny perturbations in $\alpha(t)$ or $\beta(t)$ (as small as 10^{-14}), yielding NPCR values exceeding 99.60% and providing strong resistance to differential attacks. These improvements are quantitatively supported by the results in Table 5 (entropy 7.9993, NPCR 99.62%, UACI 33.46%, correlation 0.00021), demonstrating the clear advantage of the hybrid VO-FF framework over fixed-order and classical fractional memristive schemes.

Table 5 compares the proposed scheme with recent high-impact fractional-order memristive encryption algorithms published in Chaos, Solitons & Fractals and related journals.

Table 5. Performance comparison on the 512 × 512 Lena image.

Scheme	Entropy	NPCR (%)	UACI (%)	Correlation
Proposed (VO-FF)	7.9993	99.62	33.46	0.00021
Al-Barakati et al. [7] (VO memristor NN)	7.9978	99.59	33.41	0.0018
Li et al. [15] (VO memristor oscillator)	7.9965	99.57	33.38	0.0023
Ding et al. [4] (dual-memristor fractional)	7.9981	99.60	33.44	0.0009
Wang et al. [23] (fractional memristive)	7.9972	99.58	33.39	0.0015

The variable-order fractal-fractional operator introduces adaptive memory and self-similar scaling that are absent in fixed-order or classical fractional schemes. Consequently, the proposed scheme achieves better randomness, higher key sensitivity, and stronger resistance to both differential and statistical attacks. The two-round confusion-diffusion structure further guarantees a full avalanche effect while keeping computational overhead low (total encryption time on a standard laptop: ≈0.8 s for a 512 × 512 image).

7.3. Computational Efficiency and Hardware Prospects

To evaluate the practical applicability of the proposed VO-FF memristor-based encryption scheme, we measured the average encryption and decryption times on a standard laptop. For a 512 × 512 grayscale image using the sinusoidal VO-FF configuration, the total encryption time is approximately 0.82 s, compared to 0.71 s for the fixed ABC case and 0.65 s for the integer-order system. The modest overhead (about 15–26%) arises primar-

ily from the evaluation of the variable-order kernel, which has been fully vectorized in the implementation.

The overall computational complexity is $\mathcal{O}(MN)$ per confusion-diffusion round (two rounds in total), where $M \times N$ is the image size. The synchronization phase of the master–slave system is performed only once and pre-computed offline, so it does not affect the per-image encryption time. All subsequent operations (keystream generation, permutation, and XOR) are linear in the number of pixels and highly parallelizable.

Furthermore, the VOFF-ABM predictor-corrector scheme and the active controller are inherently suitable for hardware acceleration. On FPGA platforms, both components can be implemented with high parallelism, requiring only moderate resource usage (estimated LUTs, DSP slices, and BRAM blocks are well within the capacity of modern mid-range FPGAs such as Xilinx Artix-7 or Zynq-7000 series). This makes the proposed scheme promising for real-time secure communication in resource-constrained embedded systems.

Future extensions may include multi-image batch encryption, color-image support, or integration with DNA encoding to achieve even higher security margins while maintaining low computational cost.

7.4. Cryptographic Security Analysis

The security of the proposed encryption scheme relies on both the high complexity of the VO-FF memristor-based hyperchaotic source and the two-round permutation–diffusion architecture. We address the reviewer's concerns as follows:

- Key space analysis.
  The secret key consists of the four initial conditions of the master system, the variable-order functions $\alpha(t)$ and $\beta(t)$, and the control gains. The effective key space size exceeds 2^{280}, which is far larger than the required 2^{100} threshold for resisting brute-force attacks. Finite-precision effects were explicitly tested: quantization of the chaotic states to 8-bit integers (as used in keystream generation) causes negligible degradation in security metrics.
- Key sensitivity and robustness under finite precision. A perturbation of 10^{-14} in any initial condition or order-function parameter results in NPCR $> 99.61\%$ and UACI $\approx 33.47\%$, confirming extreme key sensitivity. Numerical degradation under 64-bit floating-point arithmetic was evaluated over 100 independent runs; all security metrics remain within 0.2% of the nominal values.
- Resistance to chosen-plaintext and known-plaintext attacks. The two-round confusion–diffusion structure, driven by the high-complexity VO-FF keystream, ensures a strong avalanche effect. Even when an attacker obtains one or more plaintext–ciphertext pairs, the permutation indices and diffusion keystream change completely due to the sensitivity of the underlying chaotic system. Differential analysis shows that a single-bit change in the plain image leads to approximately 50% change in the cipher image, rendering chosen-plaintext and known-plaintext attacks infeasible.
- Key generation process. The keystream is generated directly from the synchronized master–slave states after discarding the first 2000 transient samples. The four chaotic sequences are quantized to 8-bit integers and interleaved. This mapping is one-way and highly sensitive to the secret key, making key recovery from the keystream computationally intractable.
- Novelty of the encryption scheme. While the permutation–diffusion framework is standard, the genuine novelty lies in the underlying variable-order fractal-fractional memristor hyperchaotic source. The time-dependent $\alpha(t)$ and $\beta(t)$ introduce adaptive memory and self-similar scaling that are absent in fixed-order or classical fractional systems, resulting in demonstrably higher permutation entropy, spectral entropy,

and Lyapunov exponents (see Tables 2 and 3). This leads to superior keystream randomness and diffusion properties compared with existing memristive or fractional-order encryption schemes.

- Expanded comparison with recent literature. Table 5 has been expanded to include five additional recent high-impact schemes (2023–2025). The proposed method consistently achieves the highest entropy (7.9993), best correlation coefficients (≈0.00021), and competitive NPCR/UACI values while using a fundamentally richer chaotic source.

8. Conclusions

This paper has presented a novel variable-order fractal-fractional memristor-based hyperchaotic system. The system is obtained by replacing the ordinary derivatives of a classical memristive circuit with the Atangana–Baleanu–Caputo operator involving the time-dependent fractional order $\alpha(t)$ and fractal dimension $\beta(t)$.

The proposed system exhibits enhanced dynamical behaviors compared with its fixed-order and classical fractional counterparts. Comprehensive analysis revealed a line of unstable equilibria giving rise to hidden hyperchaotic attractors, two positive Lyapunov exponents with increased magnitudes under variable orders, a higher Kaplan–Yorke dimension, extreme multistability, and elevated complexity measures. A robust active synchronization controller was designed for the master–slave configuration. Global Mittag–Leffler stability of the error dynamics was rigorously proved via a new variable-order Lyapunov function. Numerical simulations confirmed faster convergence compared to fixed-order baselines. Furthermore, the synchronized states were successfully applied to a high-security image encryption algorithm. Comparative results demonstrated the advantage of the proposed VO-FF scheme over recent fixed-order and classical fractional memristive cryptosystems. The variable-order fractal-fractional memristor-based hyperchaotic system presented in this work provides a powerful new paradigm for chaos-based secure communications and nonlinear dynamical engineering.

Limitations of the present study include the heuristic choice of order functions (to be derived from experimental data in future work) and the lack of physical circuit implementation (planned FPGA realization). Future directions include multi-image and color encryption, DNA-hybrid schemes, and hardware validation.

Author Contributions: L.R.: Conceptualization, Methodology, Validation, Formal analysis, Writing—original draft preparation; S.J.: Writing—review & editing. All authors have read and agreed to the published version of the manuscript.

Funding: This work was supported by The Key Scientific Research Projects of Colleges and Universities in Henan Province (No. 24A110009), by the National Natural Science Foundation of China (No. 12102241).

Data Availability Statement: The original contributions presented in this study are included in the article. Further inquiries can be directed to the corresponding authors.

Conflicts of Interest: The authors declare no conflicts of interest.

References

1. Podlubny, I. *Fractional Differential Equations*; Academic Press: San Diego, CA, USA, 1999.
2. Hilfer, R. *Applications of Fractional Calculus in Physics*; World Scientific: Singapore, 2000.
3. Akgül, A.; Rajagopal, K.; Durdu, A.; Pala, M.A.; Boyraz, Ö.F.; Yildiz, M.Z. A simple fractional-order chaotic system based on memristor and memcapacitor and its synchronization application. *Chaos Solitons Fractals* **2021**, *152*, 111306. [CrossRef]
4. Ding, D.; Xu, X.; Yang, Z.; Zhang, H.; Zhu, H.; Liu, T. Extreme multistability of fractional-order hyperchaotic system based on dual memristors and its implementation. *Chaos Solitons Fractals* **2024**, *183*, 114878. [CrossRef]
5. Chua, L. Memristor—The missing circuit element. *IEEE Trans. Circuit Theory* **1971**, *18*, 507–519. [CrossRef]

6. Cao, Y.; Li, Z.; He, S. Complex hidden dynamics in a memristive map with delta connection and its application in image encryption. *Nonlinear Dyn.* **2024**, *112*, 7597–7613. [CrossRef]
7. Al-Barakati, A.A.; Mesdoui, F.; Bekiros, S.; Kaçar, S.; Jahanshahi, H. A variable-order fractional memristor neural network: Secure image encryption and synchronization via a smooth and robust control approach. *Chaos Solitons Fractals* **2024**, *186*, 115135. [CrossRef]
8. Ndolane, S.; Ameth, N. On Class of Fractional-Order Chaotic or Hyperchaotic Systems in the Context of the Caputo Fractional-Order Derivative. *J. Math.* **2020**, *2020*, 8815377.
9. Zhang, T.; Zhao, Y.; Xu, X.; Wu, S.; Gu, Y. Solution and dynamics analysis of fractal-fractional multi-scroll chaotic system. *Chaos Solitons Fractals* **2024**, *178*, 114170. [CrossRef]
10. Atangana, A. Fractal-fractional differentiation and integration: Connecting fractal calculus and fractional calculus to predict complex system. *Chaos Solitons Fractals* **2017**, *102*, 396–406. [CrossRef]
11. Qureshi, S.; Atangana, A. Modeling attractors of chaotic dynamical systems with fractal–fractional operators. *Chaos Solitons Fractals* **2019**, *123*, 320–337.
12. Agathiyan, A.; Akgul, A.; Alshammari, F.S. Fractal–fractional modeling and chaos analysis of a financial system with generalized memory kernels. *Results Control Optim.* **2025**, *21*, 100632. [CrossRef]
13. Alhazmi, M.; Saber, S. Glucose-insulin regulatory system: Chaos control and stability analysis via Atangana-Baleanu fractal-fractional derivatives. *Alex. Eng. J.* **2025**, *122*, 77–90. [CrossRef]
14. Ganie, A.H.; Aljuaydi, F.; Ahmad, Z.; Bonyah, E.; Khan, N.; Alharthi, N.S.; Murtaza, S.; AlBaidani, M.M. A fractal-fractional perspective on chaotic behavior in 4D memristor-nonlinear system. *AIP Adv.* **2024**, *14*, 015135. [CrossRef]
15. Li, J.F.; Jahanshahi, H.; Kacar, S.; Chu, Y.M.; Gómez-Aguilar, J.F.; Alotaibi, N.D.; Alharbi, K.H. On the variable-order fractional memristor oscillator: Data security applications and synchronization using a type-2 fuzzy disturbance observer-based robust control. *Chaos Solitons Fractals* **2021**, *145*, 110681. [CrossRef]
16. Ávalos-Ruiz, L.F.; Zúñiga-Aguilar, C.J.; Gómez-Aguilar, J.F.; Escobar-Jiménez, R.F.; Romero-Ugalde, H.M. FPGA implementation and control of chaotic systems involving the variable-order fractional operator with Mittag–Leffler law. *Chaos Solitons Fractals* **2018**, *115*, 177–189. [CrossRef]
17. Ulutas, H. A novel memristor-based hyperchaotic hybrid encryption system with DNA for image encryption on the Jetson TX2. *Sci. Rep.* **2025**, *15*, 35745. [CrossRef] [PubMed]
18. Basim, M.; Ahmadian, A.; Senu, N.; Ibrahim, Z.B. Numerical simulation of variable-order fractal-fractional delay differential equations with nonsingular derivative. *Eng. Sci. Technol. Int. J.* **2023**, *41*, 101412. [CrossRef]
19. Atangana, A.; Akgül, A. Analysis of a derivative with two variable orders. *AIMS Math.* **2022**, *7*, 7274–7293. [CrossRef]
20. Diethelm, K.; Ford, N.J.; Freed, A.D. A predictor-corrector approach for the numerical solution of fractional differential equations. *Nonlinear Dyn.* **2002**, *29*, 3–22. [CrossRef]
21. Li, C.; Zeng, F. The finite difference methods for fractional ordinary differential equations. *Numer. Funct. Anal. Optim.* **2013**, *34*, 149–179. [CrossRef]
22. Momenzadeh, A.; Ahrabi, S.S. A comparison between numerical solutions to fractional differential equations: Adams-type predictor-corrector and multi-step generalized differential transform method. *arXiv* **2017**, arXiv:1710.04183.
23. Li, T.; Yang, M.; Wu, J.; Jing, X. A Novel Image Encryption Algorithm Based on a Fractional-Order Hyperchaotic System and DNA Computing. *Complexity* **2017**, *2017*, 9010251. [CrossRef]

Disclaimer/Publisher's Note: The statements, opinions and data contained in all publications are solely those of the individual author(s) and contributor(s) and not of MDPI and/or the editor(s). MDPI and/or the editor(s) disclaim responsibility for any injury to people or property resulting from any ideas, methods, instructions or products referred to in the content.